Characterisation of tumour immune microenvironment remodelling following oncogene inhibition in preclinical studies using an optimised imaging mass cytometry workflow

Febe van Maldegem[1,7,8], Karishma Valand[1,7], Megan Cole[1], Harshil Patel[2], Mihaela Angelova[3], Sareena Rana[1,5], Emma Colliver[3], Katey Enfield[3], Nourdine Bah[2], Victoria Siu Kwan Tsang[1], Edurne Mugarza[1], Christopher Moore[1], Philip Hobson[4], Dina Levi[4], Miriam Molina-Arcas[1], Charles Swanton[3,6], Julian Downward[1,5,8]

[1] Oncogene Biology Laboratory, [2] Bioinformatics and Biostatistics Science Technology Platform, [3] Cancer Evolution and Genome Instability Laboratory, [4] Flow Cytometry Science Technology Platform, Francis Crick Institute, 1 Midland Road, London NW1 1AT, UK

[5] Lung Cancer Group, Division of Molecular Pathology, Institute of Cancer Research, 237 Fulham Road, London SW3 6JB, UK.

[6] Cancer Research UK Lung Cancer Centre of Excellence, University College London Cancer Institute, Paul O'Gorman Building, 72 Huntley Street, London WC1E 6DD, UK

[7] These authors contributed equally

[8] Correspondence: julian.downward@crick.ac.uk, febe.vanmaldegem@crick.ac.uk

Abstract

Mouse models are critical in pre-clinical studies of cancer therapy, allowing dissection of mechanisms through chemical and genetic manipulations that are not feasible in the clinical setting. In studies of the tumour microenvironment (TME), novel highly multiplexed imaging methods can provide a rich source of information. However, the application of such technologies in mouse tissues is still in its infancy. Here we present a workflow for studying the TME using imaging mass cytometry with a panel of 27 antibodies on frozen mouse tissues. We optimised and validated image segmentation strategies and automated the process in a Nextflow-based pipeline (imcyto) that is scalable and portable, allowing for parallelised segmentation of large multi-image datasets. Incorporating user-specific plugins, imcyto can be flexibly tailored to a wide range of segmentation needs. With these methods we interrogated the dramatic remodelling of the TME induced by a KRAS G12C inhibitor in an immune competent mouse orthotopic lung cancer model, showcasing their potential as key discovery tools to enhance understanding of the interplay between tumour, stroma, and immune cells in the spatial context of the tissue.

Introduction

The advent of successful immune checkpoint inhibitors has revolutionised the treatment of cancer in recent years. However, a large proportion of patients exhibit intrinsic or acquired resistance, and good prognostic markers for response are lacking. The TME is thought to play a key role mediating immune evasion. Therefore, it will be crucial to enhance our knowledge about the cells infiltrating the tumour and their spatial context. Manipulating the TME to revert immune suppression has the potential to significantly enhance the efficacy of immunotherapies. Mouse preclinical cancer models provide an excellent platform to study such interventions aimed at the TME in a controlled manner.

In recent years, with the use of multiplex techniques such as single cell mass cytometry (CyTOF) and single cell RNA sequencing, it has become apparent that tumours are infiltrated with a diverse spectrum of immune cells, often with different phenotypes from their normally homeostatic counterparts[1, 2]. Unfortunately, the digestion of the tissue that is required to perform such analysis destroys the spatial context of the TME. Immunofluorescence (IF) and immunohistochemistry can provide spatial localisation data, but the number of markers that can be used simultaneously is limited by the spectral overlap of fluorophores and chromogens. Thus, novel highly multiplexed imaging technologies, such as imaging mass cytometry (IMC) that is based on unique atomic mass not wavelength, are extremely attractive, allowing for in depth characterisation of the TME with a metal-conjugated antibody panel of up to 40 markers while retaining the spatial context[3, 4].

While products and methods for conducting IMC studies on patient samples are becoming well established, publications using IMC in the mouse are scarce and use limited antibody complexity without subsequent quantification of the images[5, 6]. Here we present a complete IMC workflow, including a validated 27-marker antibody panel, automated and optimised image segmentation using our imcyto pipeline, and showcasing various spatial analyses. We applied these methods to study the effects of MRTX1257, a mutant specific inhibitor of the KRAS G12C oncoprotein, on the TME of an immunotherapy refractory KRAS G12C mutant lung cancer. The targeted inhibition of oncogenic KRAS signalling using the recently developed mutant specific

KRAS G12C covalent inhibitors has shown very promising efficacy in reports of currently ongoing phase 1 and phase 2 clinical trials in KRAS G12C mutant lung cancer[7, 8]. However, it is expected that long term therapeutic responses will be limited by acquisition of drug resistance, and therefore combination therapies are under intense investigation. A recent study reported enhanced survival when combining the KRAS G12C inhibitor AMG510 with anti-PD1 immune checkpoint blockade in an immunotherapy sensitive syngeneic KRAS G12C mutant CT26 colon carcinoma subcutaneous tumour model[9]. This prompted us to investigate the effects of tumour-specific KRAS inhibition on the TME in the context of a preclinical model of lung cancer.

Using IMC, we have gained in-depth and quantitative insight into the phenotypes and spatial relationships of immune cells and stromal compartments of the mouse lung TME, and how KRAS G12C inhibition promotes remodelling into a more immune activated state.

Results

An antibody panel for imaging mass cytometry on mouse tissues

Due to the limited availability of antibodies that are well validated for use on mouse formalin-fixed and paraffin-embedded (FFPE) tissues, especially with respect to immunology markers, we designed and validated a 27-antibody panel for use on frozen tissue sections. Example composite images are shown in Figure 1a and Supplemental Figure 1.

With this panel we are able to distinguish many different immune cell types that are thought to play a role in the TME, such as lymphocytes and various subsets of myeloid cells. In addition, this panel included markers to visualise the context of the tissue architecture, e.g. endothelium and fibroblasts, as well as phenotypic markers that describe maturation and activation state of both tumour and immune cells (Figure 1b and Supplemental Table 1). Twelve metals remain free for insertion of additional markers to customise this panel, with several slots in the most sensitive range of the detector, suitable for dimmer markers such as additional checkpoint molecules.

Targeted inhibition of KRAS G12C in a preclinical model of lung cancer

Orthotopic transplants of the 3LL ΔNRAS cell line, a KRAS G12C mutant and NRAS-knockout Lewis Lung Carcinoma derivative that we previously shown to be sensitive to KRAS G12C inhibition[10], were treated for seven days with the KRAS G12C inhibitor MRTX1257 or vehicle, before lungs were harvested, processed and stained with our antibody panel. In marked contrast to CT26, the Lewis Lung Carcinoma is considered to be highly refractory to immune interventions[11] and has an immune cold, or immune excluded, phenotype. Treatment of 3LL ΔNRAS tumours established in the lungs with the KRAS G12C inhibitor MRTX1257 very markedly limited tumour growth over a period of seven days, compared to control mice, although most tumours did not actually reduce in size (Supplemental Figure 2).

A total of twelve tumours were selected for IMC, six tumours from three mice of each treatment group. At first inspection, the images revealed recurrent patterns in the cellular arrangement of the tissues (Figure 1c). Vehicle treated tumours usually

showed a tissue architecture in which CD68$^+$ macrophages accumulated along the edge of the tumour, while F4/80$^+$ and CD206$^+$ macrophages seemed more intermixed with tumour cells. Effector cells such as CD4$^+$ and CD8$^+$ T cells were mostly excluded from the tumour area. Upon treatment with MRTX1257, the tissue organisation became more diffuse, macrophage phenotypes changed, and, most dramatically, the T cells infiltrated the tumour bed.

Optimisation of single cell segmentation using cell type specific settings

Quantification of IMC data requires image segmentation to extract expression data at the single cell level. As our dataset consisted of twelve large regions of interest (ROIs), ranging from 1 to 9 mm^2, we sought a software solution that would be able to scale sufficiently and therefore chose to work with open source packages CellProfiler and Ilastik, as previously described by the Bodenmiller lab[12]. Any of the published segmentation strategies for IMC were originally optimised and validated on human FFPE tissues. Therefore, we first questioned what method would be most appropriate for use on frozen mouse tumours. In most instances, cell segmentation starts with the segmentation of the nuclei, which can subsequently be used as seeds to expand into cell objects. Various methods have been described to subsequently define the cell border: by expanding the nuclear perimeter by a fixed distance, such as 3 pixels, by a watershed method onto a membrane staining[4], or by propagation onto a probability map of membranes generated by pixel classification with machine learning[12, 13]. We started with testing two of these methods, the 3px expansion and the propagation method onto a probability map of membrane (Figure 2a). From visual inspection of the cell masks we observed several recurring problems such as the failure to capture membrane staining of large cells, and the inclusion of signal from neighbouring cells into the smaller cells such as lymphocytes. In particular the inclusion of signal from neighbouring cells (spatial “spillover”) led to increased noise in the data. In addition we observed that cells with a spindle shape, such as alpha smooth muscle actin (αSMA) expressing fibroblasts, were captured very poorly. Figure 2b shows examples of these segmentation errors resulting from 3px expansion and propagation pipelines in studying macrophages, lymphocytes and fibroblasts.

We explored modifications of these segmentation strategies with the aim to improve the quality of the data. A simple strategy to improve the signal-to-noise ratio in the

pixel expansion segmentation, was to minimise the radius by which the cells were expanded from the nucleus. A 1-pixel expansion segmentation led to a reduced contact between cell boundaries and therefore less signal bleed between neighbouring cells (Figure 2b). This was reflected in the improved signal capture ("enrichment") per cell, when considering the amount of signal capture in the brightest 500 cells for a particular marker, relative to the rest of the cells in the image (Figure 2d), as well as the improved signal/noise within individual cells (Figure 2e).

These three strategies used only one set of parameters to identify all nuclei, the seeds of each cell object. However, in complex tissues such as the TME, nuclei differ widely in size and shape. Setting a size threshold for an average tumour cell may easily exclude the smaller T cells, while stringent "declumping" settings can unnecessarily split up larger multi-lobed nuclei of tumour cells and macrophages. Also, the general absence of a clearly identifiable nucleus associated with the αSMA signal was a likely cause for the poor segmentation of fibroblasts. Therefore, we modified the propagation method, to sequentially segment the different cell types using settings that are optimal for those cells. Each of the 'segmentation layers' is based on its own probability map and can use different settings for nucleus identification. Figure 2c is a graphic explaining the different layers of the sequential segmentation pipeline. By subtracting the mask of the cells identified at each step from the primary object layer (the nuclei), we can prioritise the cell types in the order at which they are segmented. The prioritised segmentation of the smaller lymphocytes improved their signal enrichment and signal-to-noise ratios, compared to the standard propagation method. A significant improvement was also seen for the capture of the αSMA signal into segmented cells (Figure 2b, d and e).

As a further validation of segmentation quality, we measured how well each method was able to detect challenging cell types, such as small lymphocytes, irregularly shaped macrophages, and the before mentioned fibroblasts. We manually annotated a set of $CD4^+$ and $CD8^+$ T cells, $CD103^+$ dendritic cells (DCs), $F4/80^+$ macrophages and αSMA^+ fibroblasts in the image. We counted how many of the highest expressing cells identified by the different segmentation strategies overlapped with these manually annotated cells. There was an improvement in detection of T cells, macrophages and fibroblasts in the sequential segmentation dataset, as shown in

the bar graph manual annotation in Figure 2f. As a negative control we also looked at the identification of CD103^{+} DCs, which was not prioritised in the sequential segmentation pipeline using cell type specific markers, but instead was segmented at step 9 along with the bulk of the remaining cells using 1px expansion. These cells were detected to a similar extent in all four segmentation pipelines.
An added advantage of using pixel classification with Ilastik was that we could also use marker combinations to identify larger tissue structures, including tumour, normal adjacent tissue and the interface between those two. This domain segmentation added a layer of spatial context, allowing for quantification of markers and cell types within the different tissue compartments (Figure 2g).

imcyto: A Nextflow based automated pipeline for segmentation on a computing cluster

To be able to run our complex sequential segmentation method on large datasets, we developed a Nextflow-based segmentation pipeline, optimised to run on a high performance computing cluster. Nextflow is based on the concept that software does not need to be installed on a server for it to be executed. Using Docker or Singularity containers, software packages are run as virtual images and are thereby portable, reproducible and platform independent. The resulting pipelines can be parallelised to make the process scalable across large datasets[14]. For automation of our workflow, we combined IMCtools, Ilastik and CellProfiler into our Nextflow-based “imcyto” pipeline (Supplemental Figure 3). The programs take in custom settings provided in the form of user-generated Ilastik and CellProfiler project files as plugins, thereby making the pipeline adaptable to widely varying segmentation methods. As such, all of the four segmentation strategies discussed above can be run using this pipeline. Segmentation using the sequential method on our dataset consisting of 12 images ranging from 429MB up to 3.35GB, was completed in less than 45 minutes on the high performance cluster at The Francis Crick Institute.

IMC single cell analysis reveals dramatic remodelling of TME

The MRTX1257 treatment had clearly resulted in changes of phenotype and spatial organisation of cell types (Figure 1c). To interrogate the data in a more quantitative manner, we employed a collection of analysis methods, such as clustering and dimensionality reduction to characterise the cell types and their activation states. We

integrated the spatial information at the tissue level using the domain classification obtained from the sequential segmentation pipeline, while cell-cell interactions were explored using the neighbouRhood analysis developed by the Bodenmiller group[15], as well as an approach that assessed distances between cell types. Each method explores different aspects of the spatial relationships within the TME. Unsupervised clustering by Phenograph[16], followed by supervised splitting of clusters and manual annotation of cell types based on marker expression patterns, resulted in a total of 35 clusters (Figure 3a and 3b, and Supplemental Figure 4a, Supplemental methods). Grouping of the Phenograph clusters into larger metaclusters, showed that approximately 35% of cells in the dataset were tumour cells and a similar proportion was taken up by myeloid cells, predominantly macrophages. Fibroblasts and lymphocytes represented a much smaller proportion, 2.2% and 5.8% respectively (Figure 3c and Supplemental Figure 4b). Principal Component Analysis (PCA) on the mean intensities of all markers per cell showed separation of the images by treatment along the principal component axes (Supplemental Figure 4c). In particular the macrophage and fibroblast compartments were expanded by the MRTX1257 treatment, while the proportion of neutrophils appeared reduced (Figure 3c and d, Supplemental Figure 4b). The latter cell type seemed especially concentrated in patches of necrotic tumour tissue in the vehicle treated samples, while these patches were mostly absent in the MRTX1257 treated tumours (Supplemental Figure 4d). The domain distribution within the metaclusters showed large shifts in spatial organisation as a response to the treatment (Figure 3e and 3f and Supplemental Figure 4d). Many cell types had an increased presence in the tumour domain in the MRTX1257 treated samples, such as lymphocytes, which we had already observed in the raw images (Figure 1c), but also fibroblasts, DCs and blood vessels. To interactively explore the movement of the cell types between the tissue domains as a result of the treatment, we made use of a visualisation tool that sets the three main tissue domains “normal”, “tumour” and “interface” as x, y and z dimensions in a 3D plot. By connecting the averages of the two treatment groups this visualised the magnitude of shift in spatial distribution (Supplemental data 3D plot). While the MRTX1257 treatment achieved good inhibition of tumour growth over the treatment period of seven days, there was very little actual tumour regression observed. We wondered whether some of this could be attributed to the increased influx of immune cells, such as has been described in the form of pseudoprogression

or stable disease in response to immune checkpoint inhibitors[17, 18]. Comparing the relative cellularity of the main cell types between the treatments Figure 3g confirmed that the proportion of tumour cells in the tumour domain was reduced from 66% in the vehicle treated dataset to 40% in the MRTX1257 treatment group, while many immune subsets and in particular the macrophage compartment had expanded significantly.

Canon et al. previously reported changes in macrophages and T cells in response to the KRAS G12C inhibition[9]. This prompted us to investigate these cell types in more detail. Uniform Manifold Approximation and Projection for Dimension Reduction (uMAP), which better preserves the global structure in the data than tSNE[19], confirmed the relatedness of many of the macrophage Phenograph clusters (Supplemental Figure 5a). The macrophage metacluster separated out into two major macrophage subtypes that not only differed by phenotype, but also by their distribution across the tissues and how they responded to the treatment. One subset, which we called Type 1 macrophages, were mainly represented by cluster 11 and characterised by high CD68 and CD11c expression, PD-L1 expression and ribosomal protein S6 phosphorylation (pS6) (Figure 4a, b and c, Supplemental Figure 5a). By phenotype they resemble normal alveolar macrophages, but their accumulation at the tumour edge (interface domain) suggests these might be pro-inflammatory M1 tumour-associated macrophages. This macrophage subset remained fairly stable between the two treatment groups, with respect to phenotype and localisation. The second subset of macrophages, Type 2, was represented by clusters 5A, 8 and 26, and characterised by F4/80 and CD206 expression, similar to immune suppressive M2 tumour associated macrophages, and was found almost exclusively within the tumour domain (Figure 4c). This macrophage subtype expanded significantly upon KRAS inhibition. Furthermore, their phenotype changed dramatically with treatment, with increased expression of F4/80, CD206 and most notably MHC-II and CD86, indicating a maturation into antigen presenting cells (Supplemental Figure 5a). A Slingshot pseudotime trajectory analysis for this subset supported the gradual differentiation with treatment (Figure 4d).

Using CellProfiler's "Object relationships" output from our imcyto pipeline, we applied the Bodenmiller neighbouRhood analysis[15] on the two macrophage subtypes to look for cell types that would be enriched or depleted in their direct neighbourhood. Rather than looking at the number of images for which a spatial relationship was

found significant, which is the default output of this analysis, we looked at the log2-fold change in neighbourhood enrichment compared to the permutated data for each ROI, to reflect the magnitude of enrichment or depletion of cell types in each other's neighbourhoods (Figure 4e and Supplemental Figure 6). This revealed some interesting relationships, such as the consistent co-existence of Type 1 macrophages with DCs and lymphocytes, while they were being rarely found in close contact with tumour cells. Indeed, visualising these cell types showed that $CD68^+$ macrophages are found often in close proximity to T cells and $CD103^+$ DCs, particularly at the edge of the tumour (Supplemental Figure 5b). This is also true of the minority of intra-tumoural $CD68^+$ macrophages, which maintain neighbourhoods with T cells and dendritic cells. Another interesting spatial interaction was observed for the Type 2 macrophages and fibroblasts, where in particular the fibroblasts in the tumour domain were found close to Type 2 macrophages (Supplemental Figure 5c). This is in line with reports that cancer associated fibroblasts can recruit monocytes and differentiate them to M2-like tumour associated macrophages[20].

Lymphocytes are thought to be the most important effector in the anti-tumour immune response. In the work from Canon et al[9], it was noted that KRAS inhibition led to an increase in T cells in the tissue, with greater expression of the maturation and exhaustion marker PD-1. In the raw images of our mouse lung tumours we observed that T cells not only increase in numbers, but as a consequence of the treatment they were now able to migrate into the tumour domain (Figure 1c, 4f and Supplemental Figure 5d). uMAP visualisation of the T cell clusters in our dataset yielded a good separation of $CD4^+$, $CD8^+$, and regulatory T cells ($Foxp3^+$) and even a few rare gamma-delta T cells (Supplemental Figure 5e). Similar to what has been previously reported, PD-1 expression on $CD8^+$T cells was markedly increased upon KRAS inhibition. More interestingly, PD-1 expression was mostly confined to $CD8^+$ T cells within the tumour area, and not detected in the adjacent normal tissue (Figure 4g). This suggests that there is either a selective recruitment of mature T cells into the tumour domain or, perhaps more likely, a localised induction of PD-1 when T cells come into contact with the TME. Insight into which cell types come into close contact with the $CD8^+$ T cells could shed some light on this matter. The neighbouRhood analysis looks at local enrichment and depletion of cells in the direct surroundings of a cell of interest, but the correction towards a permuted dataset can

lead to a relative underrepresentation of spatial interactions with abundant cell types (Supplemental Figure 6a, b and c). To quantify in a more absolute way how the neighbourhood of the T cells changes with treatment, we decided to look at distances between cell types and frequency of those interactions. We calculated the distance of each cell to the nearest $CD8^+$T cell using Pythagoras's theorem, which gives the spectrum of proximities between cell types and works across the whole image. This approach showed that some cell types are consistently found in proximity to $CD8^+$ T cells, such as other lymphocytes, dendritic cells and Type 1 macrophages. Other cell types were found further away at baseline, but this distance was reduced when the samples were treated with MRTX1257, such as for tumour cells and Type 2 macrophages – in agreement with the relocation of T cells into the tumour domain (Figure 4h). This result suggests that $CD8^+$ T cells will come under stronger influence of tumour cells and Type 2 macrophages with treatment, which might relate to their upregulation of PD-1.

To use a more unbiased approach to dissecting the differences between vehicle and MRTX1257 treated samples, we performed multiple linear regression analysis on the mean intensities of all markers in the samples (Supplemental Table 2). As expected, active mTOR signalling as detected by the pS6 antibody showed the strongest reduction in response to MRTX1257 treatment, mainly from the inhibition of signal transduction pathways in the tumour cell clusters. Markers that were upregulated with MRTX1257 treatment included the macrophage maturation markers CD206, MHC class II, and F4/80, as discussed above, as well as the fibroblast marker αSMA. Interestingly, vimentin was the second highest coefficient in the table. Vimentin expression is the canonical marker of epithelial-to-mesenchymal transition (EMT), which has been suggested as one of the possible mechanisms of resistance to KRAS-inhibition[21, 22]. In fact, mean expression of vimentin increased for all cell types in the dataset, yet most striking was the difference seen for the blood vessels. While vehicle treated samples showed relatively low expression of vimentin on the vessels compared to other cell types, following MRTX1257 treatment it became one of the highest expressing metaclusters (Figure 4i). Upregulation of vimentin on endothelium can be a reflection of endothelium-to-mesenchymal transition[23]. However, a close inspection of the PECAM and vimentin expression in the tissues, showed only modest colocalisation of the two antibodies at the pixel level. Vimentin

is also a marker for pericytes, and while we do not have another marker in the panel that would unambiguously identify these cells, the observed expression patterns strongly suggest the presence of pericytes lining the endothelium (Figure 4j). Together with the increased presence of endothelium in the tumour (Figure 3f), the detection of pericytes points to normalisation of the vasculature of the tumour as a result of KRAS G12C inhibition and agrees well with the observation that the MRTX1257 treated samples harboured fewer necrotic patches in the tumours.

Discussion

Multiplex imaging techniques such as imaging mass cytometry are beginning to take centre stage in studies of the TME[24]. Application of this technology to pre-clinical mouse studies, however, has been lacking. Here we have described the design, optimisation and validation of a complete IMC workflow for mouse tissues. Our panel of 27 antibodies, provides a good basis for immuno-oncology studies, identifying many of the cell types of interest in the TME. An additional 12 isotopes are still available, to allow for customisation in any area of research interest, such as additional checkpoint molecules or stromal markers, or for combination with RNAscope, as was previously shown for human FFPE tissues[25].

Considering the potential differences in cell densities and quality of the frozen mouse tumour tissues compared to human FFPE, we set out to find an optimised segmentation method, critical for obtaining good quality single cell data. We tested modifications to previously published image segmentation methods and established two strategies with a better performance with respect to signal-to-noise ratios and cell identification. The 1px expansion segmentation can represent a simple strategy to obtain quick segmentation data from a new antibody panel, without the need for training the classifiers. More flexible and sensitive segmentation can be obtained with a sequential segmentation strategy, and in particular this method can provide a solution to cells that are more challenging to segment. Any of those segmentation methods can simply be applied to large datasets, using our automated image segmentation pipeline, which has been made available to the wider community via the nf-core platform (*nf-core/imcyto*). This pipeline is scalable, yet flexible, as it can be customised to work with any antibody panel or segmentation strategy.

Working with mouse tissues, we have the advantage that we can image whole tumours, which is generally not possible with human samples. Seeing the tumour as a whole provides exceptional insight into the tumour architecture, as we have seen here for the very distinct cell communities within the different areas of the tissue, such as the accumulation of effector cells and Type 1 macrophages ($CD68^+$ and $CD11c^+$) at the tumour edge whilst they were being excluded from the main body of

the tumour. While MRTX1257 is a tumour-specific inhibitor, acting only on the G12C mutant form of KRAS protein found in the tumour cells and not the wild type KRAS protein found in the cells of normal tissue, it had profound indirect effects on the TME. The study of Canon et al. used flow cytometry and immunohistochemistry to look at changes in the TME upon KRAS G12C inhibition[9]. The main changes they observed were increases in macrophage, DCs and T cells. Our data confirmed those observations and provided additional spatial phenotypic data. We have used several different approaches to explore the spatial relationships between cell types, within cell neighbourhoods, and across the tissue domains. We showed how the tumour bed becomes infiltrated with maturing macrophages and PD-1$^+$ lymphocytes, changing the spatial interactions between these cells. Interestingly some cells seemed to consistently exist together, such as the Type 1 macrophages that remain within the cell neighbourhood of T cells and DCs, irrespective of whether they are in the interface or in the tumour domain. This suggests either that their recruitment is regulated by the same mechanism, or that there is a functional importance to their interaction. While the DCs in that cellular niche expressed co-stimulatory molecules such as CD86 and could therefore potentially activate the T cells, the Type 1 macrophages expressed high levels of PD-L1 and would in turn be able to repress the T cell activation. Clearly, such local interactions could be fundamental to the outcome of immunotherapeutic treatments. It also raises the question of the state of the local chemokine and cytokine milieu. While a study by Schulz, et al. demonstrated that IMC can be combined with transcript detection using an RNA-scope based in situ hybridisation[25], the detection level of cytokine mRNA is often a limiting factor. A multi-omics approach combining IMC with single cell approaches such as CITE-Seq[26], or spatial transcriptomics[27, 28] would therefore have the potential to significantly enhance our insight into the mechanisms regulating cellular communities.

A major advantage of a multiplex technology is that it allows for discovery and hypothesis generation. The finding of a higher expression of vimentin across all cell types was unanticipated but could be explained by a greater mobility of cells in the remodelling process of the TME[29]. In addition, it led to the observation that there was an increased presence of endothelium and possibly pericytes, pointing towards normalisation of the tumour vasculature upon MRTX1257 treatment in this normally haemorrhagic and necrotic tumour model[30]. Altogether, our data shows that

treatment with a tumour-specific KRAS inhibitor can dramatically remodel the TME in favour of an anti-tumour immune response, even in an immune cold tumour model such as the 3LL Lewis Lung Carcinoma. Current investigations are aimed at elucidating the mechanism by which this conversion is mediated.

We have presented here a complete IMC workflow for use in preclinical mouse studies and demonstrated the value and importance of using IMC to study the effects of a treatment on the spatial organisation of the TME.

Methods

In vivo drug study

This work was performed under a UK Home office approved project license and in accordance with institutional welfare guidelines. 10^6 3LL ΔNRAS Lewis Lung Carcinoma cells[10] were injected in the tail vein of 9-11 week old C57BL/6 mice and allowed to establish for 3 weeks. The lung tumour burden was assessed using a Quantum GX2 microCT Imaging System (PerkinElmer) and treatment groups were randomised with stratification by tumour number and size. MRTX1257 was prepared by sonication in 10% Captisol® (Ligand) and 50 mM citrate buffer (pH 5.0) and administered daily at 50mg/kg by oral gavage (5μg/g) for 7 days. At day 8 mice were scanned again and sacrificed with a terminal overdose (0.1ml/10g body weight intraperitoneal) of a mixture of Pentobarbital (2% w/v) and Mepivacaine hydrochloride (8 mg/ml), followed by cervical dislocation.

Tumour volume measurements

Mice were scanned before start of treatment and at the end of treatment using a Quantum GX2 microCT Imaging System (PerkinElmer), while mice were held under isoflurane anaesthesia. Tumour volume were measured using AnalyzeDirect software. Tumours with a minimum starting size of 0.4mm^3 at the time of the first scan were included in the analysis.

Tissue processing

Three mice from both the vehicle and the MRTX1257 treated group were processed to be used in IMC. Dissected lungs with tumours were stored in 20% ice cold sucrose up to one hour before embedding in Tissue-Tek O.C.T. Compound (Sakura) and being frozen gently using an isopentane liquid nitrogen bath. Blocks were stored at -80C until further processing.

Antibody staining

Five μm thin tissue sections were cut and collected on SuperFrost Plus™ Adhesion slides (Thermo Scientific) in a cryostat and stored at -80°C. When required, slides were thawed for 3 hours, fixed for 10 min with Image-iT™ Fixative Solution

(ThermoFisher) and washed with DPBS (GIBCO) and then DPBS/0.05%Tween. Slides were blocked with Superblock blocking buffer in DPBS (Thermo Scientific) for 30 min and then 1:100 anti-CD16/CD32 FC-block (BD Biosciences) for 10 min. Staining was done with a cocktail of primary antibodies in 0.5% BSA and 1:100 anti-CD16/CD32 FC-block in DPBS/0.05%Tween for 1 hour in a dark humid chamber and followed by washings in DPBS/0.05%Tween and then DPBS alone three times each and rinsed in MilliQ water. For immunofluorescence (IF) the samples were then mounted with ProLong Gold Antifade Mountant with/without DAPI (Thermo Scientific), coverslipped and left to air dry overnight. For IMC, after the final DPBS wash slides were incubated with 1:500 Cell-ID Intercalator-Ir (Fluidigm) in DPBS for 10 min and rinsed with MilliQ water before air drying overnight. Antibody clones conjugated with metal isotopes were purchased from Fluidigm where available (mouse CyTOF catalogue) or obtained in purified format and conjugated in house using MaxPar conjugation kits (Fluidigm) according to the manufacturer's protocol. Details of the antibodies used for IF and IMC are listed in Supplemental Table 1.

Image acquisition

IF slides were imaged with a Zeiss Upright 710 microscope with a 20x objective lens using Zen blue imaging software (Zeiss). IMC images were acquired using Hyperion Imaging Mass Cytometer. Each ROI was selected such that it would contain a whole tumour including adjacent normal tissue where possible, or, if required, they were cropped to contain a single tumour using the cropping script (see Code availability). Twelve images obtained from six mice were selected for this study, ranging 1~9 mm^2 (429Mb up to 3.35Gb).

For figures in this publication with IF or IMC images we used Fiji ImageJ v2.0.0 to make composite images of selected channels. For visualisation purposes the images were processed with an outlier removal step, filtered using a median or gaussian filter (0.5px radius) and scaled to enhance contrast. For Figure 1c the lymphocyte images were filtered using a band pass (3-40px) Fast Fourier Transformation to enhance detection of the cells.

Segmentation pipeline

The following section describes the proposed segmentation pipelines carried out in CellProfiler v3.1.9, including custom modules by Bodenmiller (https://github.com/BodenmillerGroup/ImcPluginsCP) and Ilastik v1.3.3b1 (see Code availability, and Supplemental Figure 3). In brief, data obtained as .txt files were converted into stacks of individual .tiff files per antibody marker using the IMCtools package v1.0.5 (https://github.com/BodenmillerGroup/imctools)[12]. Images in the full stack path were minimally filtered using outlier removal and median filtering in CellProfiler (both using the custom "Smooth Multichannel" module). For nuclear segmentation, images for 191Ir and 193Ir were summed, histogram equalised and segmented using a propagation-based thresholding strategy in CellProfiler.

For the pixel expansion strategy, segmented nuclei were expanded by a set number of pixels (1 or 3) to identify whole cell objects (see Figure 2a).

For the propagation strategy, selected markers (CD44, CD45, PECAM, CD11c, CD3, CD4, CD68, CD8, F480, aSMA, B220, CD206) were merged, alongside a nuclei image and converted into an RBG composite tiff in CellProfiler. This composite was fed into Ilastik pixel classification workflow and classified into nuclei, membrane and background to generate probability maps. In CellProfiler both segmented nuclei (as described) and membrane probability maps were used for whole cell segmentation using a propagation-based thresholding strategy (see Figure 2a).

Similarly, for the sequential segmentation strategy, multiple images representing individual cell types and domains were created by merging together selected markers in CellProfiler (PECAM for normal, CD44 for tumour, EPCAM and aSMA for structural, CD3, CD4, CD8 and B220 for lymphocytes, and CD68, F480, CD206 and CD11c for macrophages). These 5 new images alongside a nuclei image were combined into a 6-channel image in CellProfiler. This was fed into Ilastik autocontext workflow and classified into tissue domains (nuclei, tumour, normal, structural) and cell types (lymphocytes, macrophages, fibroblasts) to generate probability maps. In CellProfiler, individual cell types (in order - lymphocytes, macrophages, fibroblasts, normal cells, tumour cells, remaining cells) were sequentially segmented using both segmented nuclei (as described but with customised size parameters) and corresponding probability maps, with the exception of fibroblasts which were identified only using the probability map. All cell types were added together to generate a total cell mask. Domain segmentation was performed using thresholding

on domain probability maps, creating normal, tumour and structural domains. The interface domain was created from the overlap between normal and tumour domains. For CellProfiler and Ilastik project files used in these segmentation strategies, see *Data availability*.

Validation of segmentation strategies

All cells in the ROI "BRAC3438.6f_ROI1_t1_Vehicle" (in short: "02_Vehicle"), were ranked for expression of each of the markers depicted, and the top 500 highest expressing cells were selected to calculate the mean intensity for that marker within the top 500, and the remaining cells, as a measure of signal enrichment. Signal-to-noise ratios were calculated by taking the mean intensity of relevant marker in the top 500 cells, relative to the expression of "polluting" markers not expected to be expressed in these same cells.

We generated a small manually annotated dataset from the same image set as above, by recording the x and y coordinates of $CD4^+$ (n=92) and $CD8^+$ T cells (n=70), $CD103^+$ DCs (n=65), $F4/80^+$ macrophages (n=108) and $aSMA^+$ fibroblasts (n=88). Cells from the top 500 expressing CD4, CD8, CD103, F4/80 or aSMA were interrogated to determine how many cells of each matched up to cells in the annotated dataset, following the criterium that the cell centre had to fall within 5px of each other.

imcyto pipeline

An automated Nextflow based pipeline that sequentially pre-processes and segments imaging data and extracts single cell expression information (see Supplemental Figure 2). This pipeline combines Docker or Singularity containers for IMCtools, CellProfiler and Ilastik. Inputs for the pipeline are image data in the form of .mcd, .txt, or ome.tiff files, a .csv file with binary information on the channels to be included, the user-generated CellProfiler pipeline files (.cppipe) - custom CellProfiler modules need to be separately provided, and (pre-trained) Ilastik project files (.ilp). Output files from each step in the pipeline, such as raw or pre-processed TIFFs, probability maps, masks, Object relationships and measurements in the form of a .csv file will be created in an organised results folder structure. Alongside, a report is generated on the performance of the pipeline, with respect to memory and processor usage and running time for each individual processing step.

A detailed user guide can be found on: https://github.com/nf-core/imcyto

Data normalisation, scaling and clustering

Data for each ROI was normalised to mean intensity of Xenon134. To create the larger dataset, data from six control tumour ROIs and 6 MRTX1257 treated tumours were concatenated (282,837 cells in total for all twelve images combined) and channels scaled to the 99th percentile. A few small image areas containing a sudden drop in counts were excluded from the analysis, by excluding cells with X and Y coordinates falling within those areas. Mean pixel intensity of 17 specific cellular markers from the data were selected for high-dimensional, unsupervised clustering using Rphenograph[16]: αSMA, B220, CD103, CD11c, CD3, CD44, CD45, CD4, CD68, CD8, EPCAM, F480, LY6G, MHCII, NKp46, PECAM, PVR. This grouped the single-cell data into separate sub-populations based on phenotypic similarity of the chosen markers and assigned each to a cluster number using the Louvain community detection algorithm. A k input of 20 generated 30 clusters, and further manual separation into subclusters by expert gating resulted in 35 distinct sub-populations overall (see Supplemental Methods). Clusters were evaluated to associate each with a cell type based on the distribution of weighted expression of each marker. These cell types were then grouped into 9 metaclusters based on their phenotypic classification (see Supplemental Methods).

Phenotypic analysis

R implementations of tSNE (RtSNE)[31] and uMAP[32] were used for dimensionality reduction. Pseudotime analysis was done with Slingshot[33], using 26 as start cluster.

Spatial analysis

A permutation approach developed by the Bodenmiller lab was used to determine whether detected neighbour interactions between metaclusters occurred more frequently in the images than observed by randomization (https://github.com/BodenmillerGroup/neighbouRhood)[15]. Briefly, an 'objectTable' logging object, and cluster information, and 'Object relationships' listing each cell and all its identified neighbours within a 15-pixel distance, were sent through 5,000 rounds of permutation. A P-value was then calculated to determine whether the difference between average baseline and permutated neighbour interactions were

significantly different for each pairing combination of metaclusters. Significant interaction or avoidance was determined by baseline values falling above or below the distribution of permutated data, respectively. Averaged interactions for baseline versus permutation statistics from the Bodenmiller neighbouRhood analysis script were then compared for each pairing of metaclusters from every image by calculating Log2FC to determine how treatment affects neighbour interactions.
The Pythagoras's theorem was used to compute distances of each cell in the dataset to the nearest $CD8^+$ T cell, based on the x and y coordinates of the centre of the cells.

Data availability

Image files, pipeline input files, single-cell data, 3D plot and associated files are available at https://hdl.handle.net/10779/crick.c.5270621.

Code availability

The automated imcyto image segmentation pipeline built using Nextflow is available at https://nf-co.re/imcyto and https://github.com/nf-core/imcyto.
The code generated during this study for analysis of single cell IMC data following image segmentation was written for R v3.6.2 and is available at https://hdl.handle.net/10779/crick.c.5270621 and https://github.com/FrancisCrickInstitute/vanMaldegem_Valand_2021.

Acknowledgements

We thank David Barry, Leigh-Anne McDuffus, Richard Mitter and Julia Handl for helpful discussions. We thank the science technology platforms at the Francis Crick Institute including Biological Research Facility, Scientific Computing, Bioinformatics and Biostatistics, Flow Cytometry, Experimental Histopathology, Advanced Light Microscopy, and Cell Services.

Funding: This work was supported by funding to J.D. from the Francis Crick Institute—which receives its core funding from Cancer Research UK (FC001070), the UK Medical Research Council (FC001070), and the Wellcome Trust (FC001070)—from the European Research Council Advanced Grant RASImmune, from a Wellcome Trust Senior Investigator Award 103799/Z/14/Z, and from a Cancer Research UK Cancer ImmunoTherapy Accelerator Award (CITA-CRUK; C33499/A20265). KE was supported by a Marie Skłodowska-Curie Actions Individual Fellowship.

Author contributions: F.v.M., K.V., M.C., M.M-A., C.S., J.D. designed the study, interpreted the results and wrote the manuscript. F.v.M., K.V., M.M-A., V.T., S.R. performed the biochemical experiments. C.M., E.M., assisted with in vivo studies. F.v.M., K.V., M.C., H.P., N.B., M.A., E.C. performed computational analyses and set up the pipeline. P.H., D.L. carried out IMC analysis. M.A., K.E., E.C. provided image analysis expertise. All authors contributed to manuscript revision and review.

Competing interests: J.D. has acted as a consultant for AstraZeneca, Bayer, Jubilant, Theras, Vividion and Novartis, and has funded research agreements with BMS, Revolution Medicines and Boehringer Ingelheim. C.S. receives grant support from Archer Dx, AstraZeneca, Boehringer–Ingelheim and Ono Pharmaceutical; has consulted for AstraZeneca, Bicycle Therapeutics, Celgene, Genentech, GRAIL, GSK, Illumina, Medicxi, MSD, Novartis and the Sarah Cannon Research Institute; receives grant support and has consulted for Bristol Myers Squibb, Pfizer and Roche–Ventana; is an advisory board member and is involved in trials sponsored by AstraZeneca; has stock options in Apogen Biotechnologies, Epic Sciences, GRAIL; and has stock options and is a co-founder of Achilles Therapeutics. The other authors declare that they have no competing interests.

References:

1. Bendall, S.C. *et al.* Single-cell mass cytometry of differential immune and drug responses across a human hematopoietic continuum. *Science* **332**, 687-696 (2011).

2. Lavin, Y. *et al.* Innate Immune Landscape in Early Lung Adenocarcinoma by Paired Single-Cell Analyses. *Cell* **169**, 750-765 e717 (2017).

3. Ijsselsteijn, M.E., van der Breggen, R., Farina Sarasqueta, A., Koning, F. & de Miranda, N. A 40-Marker Panel for High Dimensional Characterization of Cancer Immune Microenvironments by Imaging Mass Cytometry. *Front Immunol* **10**, 2534 (2019).

4. Giesen, C. *et al.* Highly multiplexed imaging of tumor tissues with subcellular resolution by mass cytometry. *Nat Methods* **11**, 417-422 (2014).

5. Uraki, R. *et al.* Aedes aegypti AgBR1 antibodies modulate early Zika virus infection of mice. *Nat Microbiol* **4**, 948-955 (2019).

6. Brahler, S. *et al.* Opposing Roles of Dendritic Cell Subsets in Experimental GN. *J Am Soc Nephrol* **29**, 138-154 (2018).

7. Hallin, J. *et al.* The KRAS(G12C) Inhibitor MRTX849 Provides Insight toward Therapeutic Susceptibility of KRAS-Mutant Cancers in Mouse Models and Patients. *Cancer Discov* **10**, 54-71 (2020).

8. Hong, D.S. *et al.* KRAS(G12C) Inhibition with Sotorasib in Advanced Solid Tumors. *N Engl J Med* **383**, 1207-1217 (2020).

9. Canon, J. *et al.* The clinical KRAS(G12C) inhibitor AMG 510 drives anti-tumour immunity. *Nature* **575**, 217-223 (2019).

10. Molina-Arcas, M. *et al.* Development of combination therapies to maximize the impact of KRAS-G12C inhibitors in lung cancer. *Sci Transl Med* **11** (2019).

11. Mosely, S.I. *et al.* Rational Selection of Syngeneic Preclinical Tumor Models for Immunotherapeutic Drug Discovery. *Cancer Immunol Res* **5**, 29-41 (2017).

12. Zanotelli, V.R.T. & Bodenmiller, B. A flexible image segmentation pipeline for heterogeneous multiplexed tissue images based on pixel classification. 2019 [cited]Available from: https://github.com/BodenmillerGroup/ImcSegmentationPipeline/blob/development/documentation/imcsegmentationpipeline_documentation.pdf

13. Berg, S. *et al.* ilastik: interactive machine learning for (bio)image analysis. *Nat Methods* **16**, 1226-1232 (2019).

14. Ewels, P.A. *et al.* The nf-core framework for community-curated bioinformatics pipelines. *Nature Biotechnology* **38**, 276-278 (2020).

15. Schapiro, D. *et al.* histoCAT: analysis of cell phenotypes and interactions in multiplex image cytometry data. *Nat Methods* **14**, 873-876 (2017).

16. Levine, J.H. *et al.* Data-Driven Phenotypic Dissection of AML Reveals Progenitor-like Cells that Correlate with Prognosis. *Cell* **162**, 184-197 (2015).

17. Chiou, V.L. & Burotto, M. Pseudoprogression and Immune-Related Response in Solid Tumors. *J Clin Oncol* **33**, 3541-3543 (2015).

18. Di Giacomo, A.M. *et al.* Therapeutic efficacy of ipilimumab, an anti-CTLA-4 monoclonal antibody, in patients with metastatic melanoma unresponsive to prior systemic treatments: clinical and immunological evidence from three patient cases. *Cancer Immunol Immunother* **58**, 1297-1306 (2009).

19. Becht, E. *et al.* Dimensionality reduction for visualizing single-cell data using UMAP. *Nat Biotechnol* **37**, 38-44 (2019).

20. Gok Yavuz, B. *et al.* Cancer associated fibroblasts sculpt tumour microenvironment by recruiting monocytes and inducing immunosuppressive PD-1(+) TAMs. *Sci Rep* **9**, 3172 (2019).

21. Adachi, Y. *et al.* Epithelial-to-Mesenchymal Transition is a Cause of Both Intrinsic and Acquired Resistance to KRAS G12C Inhibitor in KRAS G12C-Mutant Non-Small Cell Lung Cancer. *Clin Cancer Res* **26**, 5962-5973 (2020).

22. Singh, A. *et al.* A gene expression signature associated with "K-Ras addiction" reveals regulators of EMT and tumor cell survival. *Cancer Cell* **15**, 489-500 (2009).

23. Piera-Velazquez, S. & Jimenez, S.A. Endothelial to Mesenchymal Transition: Role in Physiology and in the Pathogenesis of Human Diseases. *Physiol Rev* **99**, 1281-1324 (2019).

24. Baharlou, H., Canete, N.P., Cunningham, A.L., Harman, A.N. & Patrick, E. Mass Cytometry Imaging for the Study of Human Diseases-Applications and Data Analysis Strategies. *Front Immunol* **10**, 2657 (2019).

25. Schulz, D. *et al.* Simultaneous Multiplexed Imaging of mRNA and Proteins with Subcellular Resolution in Breast Cancer Tissue Samples by Mass Cytometry. *Cell Syst* **6**, 25-36 e25 (2018).

26. Stoeckius, M. *et al.* Simultaneous epitope and transcriptome measurement in single cells. *Nat Methods* **14**, 865-868 (2017).

27. Merritt, C.R. *et al.* High multiplex, digital spatial profiling of proteins and RNA in fixed tissue using genomic detection methods. *bioRxiv* **February 22, 2019** (2019).

28. Ståhl, P.L. *et al.* Visualization and analysis of gene expression in tissue sections by spatial transcriptomics. *Science* **353**, 78-82 (2016).

29. Battaglia, R.A., Delic, S., Herrmann, H. & Snider, N.T. Vimentin on the move: new developments in cell migration. *F1000Res* **7** (2018).

30. Raza, A., Franklin, M.J. & Dudek, A.Z. Pericytes and vessel maturation during tumor angiogenesis and metastasis. *Am J Hematol* **85**, 593-598 (2010).

31. Van der Maaten, L.J.P. & Hinton, G.E. Visualizing High-Dimensional Data Using t-SNE. *Journal of Machine Learning Research* **9**, 2579-2605 (2008).

32. McInnes, L., Healy, J. & Melville, J. UMAP: Uniform Manifold Approximation and Projection for Dimension Reduction. *ArXiv* (2018).

33. Street, K. *et al.* Slingshot: Cell Lineage and Pseudotime Inference for Single-Cell Transcriptomics. *bioRxiv* (2017).

Figure Legends

Figure 1. A 27 multiplex antibody panel to characterise the TME in mouse frozen tissues

a. Validation of antibodies in IMC using a tissue with known staining patterns, an example shown here is a follicle in the spleen; Ir191/193 (blue), B220 (green); CD4 (magenta), CD68 (yellow), αSMA (cyan), vimentin (red).

b. Panel of 27 antibodies that identify multiple cell types from lymphoid, myeloid, tumour and stromal compartments, as well as markers of activation and proliferation status. Detailed information on the antibody clones and isotope conjugations can be found in Supplemental table 1.

c. 3LL lung tumours, either treated with vehicle or MTRX1257 for 7 days. Overall tissue organisation changes upon KRAS-inhibition, with increased $CD45^+$ leukocytes and αSMA^+ fibroblasts in the tumour domain (left), increased expression of macrophage markers such as F4/80 and CD206 in the tumour (middle), and more T cells infiltrating the tumour bed (right). To enhance visualisation of the small lymphocytes, the channels for CD3, CD4, CD8 and B220 were filtered using a band pass Fast Fourier Transformation.

Figure 2. Comparing four segmentation strategies

a. Graphic describing pixel expansion and propagation segmentation strategies performed in CellProfiler. Identified nuclei are expanded on by a select number of pixels to create a cell mask with the pixel expansion strategy. The propagation strategy uses both identified nuclei and a membrane probability map generated by pixel classification in Ilastik to create a cell mask, using the propagation thresholding parameter in CellProfiler.

b. Representative false colour images of F4/80 (green), CD4 (yellow) and aSMA (red) markers merged with a nuclear stain (blue) and cropped (top row). Cell mask outlines (white) overlaid onto these markers were generated by either 3px expansion strategy (2nd row) or propagation strategy (3rd row), 1px expansion strategy (4^{th} row) or sequential segmentation (bottom panel). Image processing for visualisation: outliers were removed and a median filter of 0.5px radius was applied in Fiji.

c. Schematic of the sequential segmentation pipeline. Each step uses custom size threshold settings for nucleus detection, as well as cell type specific markers to generate the probability maps for membranes in Ilastik. A propagation step as described in (a) is subsequently used to find cell boundaries in steps 1, 2, 4, 5, 7. At every level, the identified objects are subtracted from the total remaining nuclei. Any remaining cells at step 9 are segmented using 1px expansion. Steps 3, 6, 8 and 10 describe the segmentation of tissue domains, based on probability maps in Ilastik.
d. Heatmap showing enrichment of markers as a result of each segmentation strategy. Enrichment was defined as the relative expression in the top 500 cells, of the markers as listed on the x-axis, compared to the expression of those same markers in the rest of the cells in the dataset.
e. Heatmap depicting the relative amount of noise in each segmentation strategy by looking at the relative expression of the key identifying marker, compared with markers that would not be expressed on the same cell, but may be found in its direct proximity within the tissue and thus would be a sign of signal bleed from adjacent cells ("signal/noise").
f. Percentage of cells from the manually annotated dataset that were matched with cells in the top 500 for each marker, compared between segmentation strategies. Size of annotated datasets: $CD103^+$ DCs, n=65 ; $CD4^+$ T cells, n=92 ; $CD8^+$ T cells, n=70; $F4/80^+$ macrophages, n=108; αSMA^+ fibroblasts, n=130.
g. Graphic showing the result of the domain segmentation as part of the sequential segmentation method, red = normal tissue, purple = tumour, green = interface, cyan = structural domain. Violin plot: Quantification of two key markers PECAM and CD44 used as the basis for the domain segmentation.

Figure 3. Characterisation and spatial distribution of cell types in Lewis Lung carcinoma model

a. Phenograph clustering using a k-value of 20 resulted in 30 clusters. Additional manual gating was done on a few remaining mixed phenotype clusters, resulting in a total of 35 clusters (see Supplemental Methods). Where clusters were split, this has been indicated by the addition of a letter to the cluster number. Heatmap showing the relative expression of all 27 markers within these 35 Phenograph clusters.
b. t-distributed stochastic neighbour embedding (tSNE) coloured by the clusters shown in a.

c. tSNE coloured by manually grouped metaclusters (see Supplemental Methods on assignment of clusters to metaclusters).
d. tSNE coloured by treatment.
e. tSNE coloured by tissue domain.
f. Relative distribution of metaclusters within the tissue domains, separated by the two treatments. It shows how the fibroblasts, lymphocytes, DCs and macrophages have increased presence in the tumour domain, while neutrophils have been reduced.
g. Proportions of metaclusters within the tumour domain, separated by treatment.

Figure 4. Impact of tumour-specific KRAS G12C inhibition on phenotype and spatial characteristics of cells in the TME

a. uMAP of macrophage clusters separates into two distinct populations. See Supplemental Figure 4 for more detailed expression profiles of the macrophage uMAP
b. Type 1 and Type 2 macrophages are best contrasted by the expression of CD68 and F4/80.
c. Tissue distribution for both macrophages differs little between treatments. Stacked bar graph showing the distribution of the two macrophage types within the tissue domains. Type 1 macrophages are found mostly in the normal and interface domain. Type 2 macrophages are found almost exclusively in the tumour domain.
d. uMAP showing the Type 2 macrophages coloured by treatment, with the curve depicting the pseudotime trajectory.
e. As the macrophages are found within different tissue domains, they also reside within a different cellular neighbourhood. Log2 fold changes in enrichment from the neighbouRhood analysis (Bodenmiller) for Type 1 and Type 2 macrophages, at the level of metaclusters (see methods). Filled circles represent images for which the enrichment was statistically significant ($p<0.01$), while open circles indicate non-significance. Values above zero indicate enrichment of a cell type in the neighbourhood of the macrophages, below zero means depletion.
f. $CD4^+$ and $CD8^+$ T cells have an increased presence in the tumour domain upon MRTX1257 treatment.
g. $CD8^+$ T cells upregulate PD-1 upon MRTX1257 treatment, but only those within the tumour domain. Histograms plotting the normalised counts for mean intensity of

PD-1 per CD8$^+$ T cell, left plot: data separated by treatment, right plot: CD8$^+$ T cells from MRTX1257treated samples only, separated by tissue domain.

h. Box-and-whiskers plot depicting the distance of metaclusters to the nearest CD8$^+$ T cell. In vehicle treated tumours, CD8$^+$ T cells are found in proximity of other lymphocytes, endothelium, DCs and Type 1 macrophages, but not close to tumour, fibroblasts, or Type 2 macrophages. Upon MRTX1257 treatment, these distances become shorter, reflective of migration of CD8$^+$ T cells into the tumour domain accompanied by increased presence of Type 2 macrophages and fibroblasts within the tumour. Boxes indicate 1st and 3rd quartile, split by the median, hinges depict 1.5*interquartile range, dots are individual outliers.

i. Violin plot showing the expression of vimentin on the metaclusters, separated by treatment. Means indicated with a dot.

j. Crop of PECAM and vimentin expression in a tumour treated with MRTX1257. For visualisation purposes, the images were processed in Fiji with a median filter (radius 0.5).

a

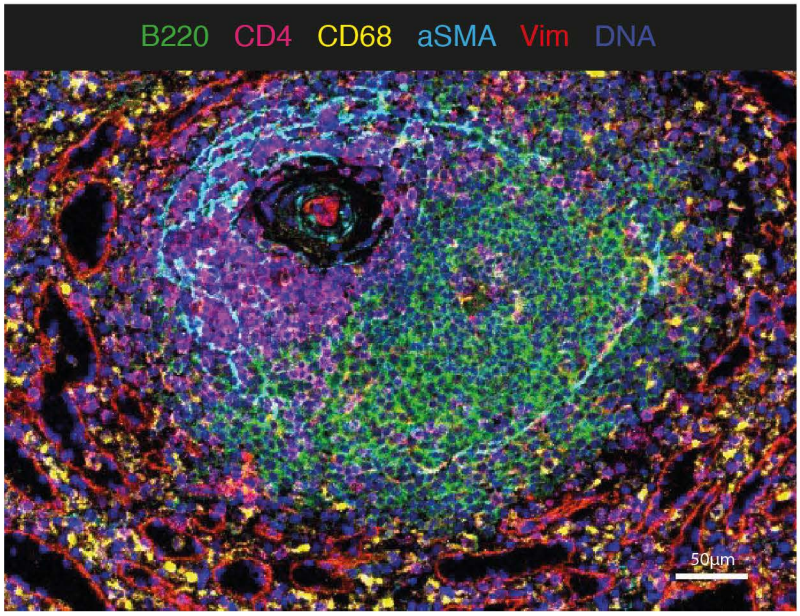

b

Lymphocytes	
CD45	Pan Leukocyte
CD3	Pan T cell
CD4	T_H cell
CD8	CytT cell
γδTCR	γδT cell
Foxp3	Regulatory T
B220	B cells
Nkp46	NK cell
PD-1	Immune checkpoint

Tumour cells	
CD44	Stemness
Vimentin	Mesenchymal
Ki67	Proliferation
casp3	Apoptosis
pS6	mTOR
PVR	TIGIT receptor

Myeloid Cells	
CD45	Pan Leukocyte
Ly6-G	Neutrophils
F4/80	Pan macrophage
CD68	Pan macrophage
CD206	"M2" macrophage
CD11c	DC/macrophages
CD103	cDC1
MHC-II	DC/APC
CD86	Co-stimulation
PD-L1	Immune checkpoint

Stroma	
EPCAM	Bronchioles /epithelial tumour
aSMA	Blood vessels /fibroblasts
CD31	Endothelium

c

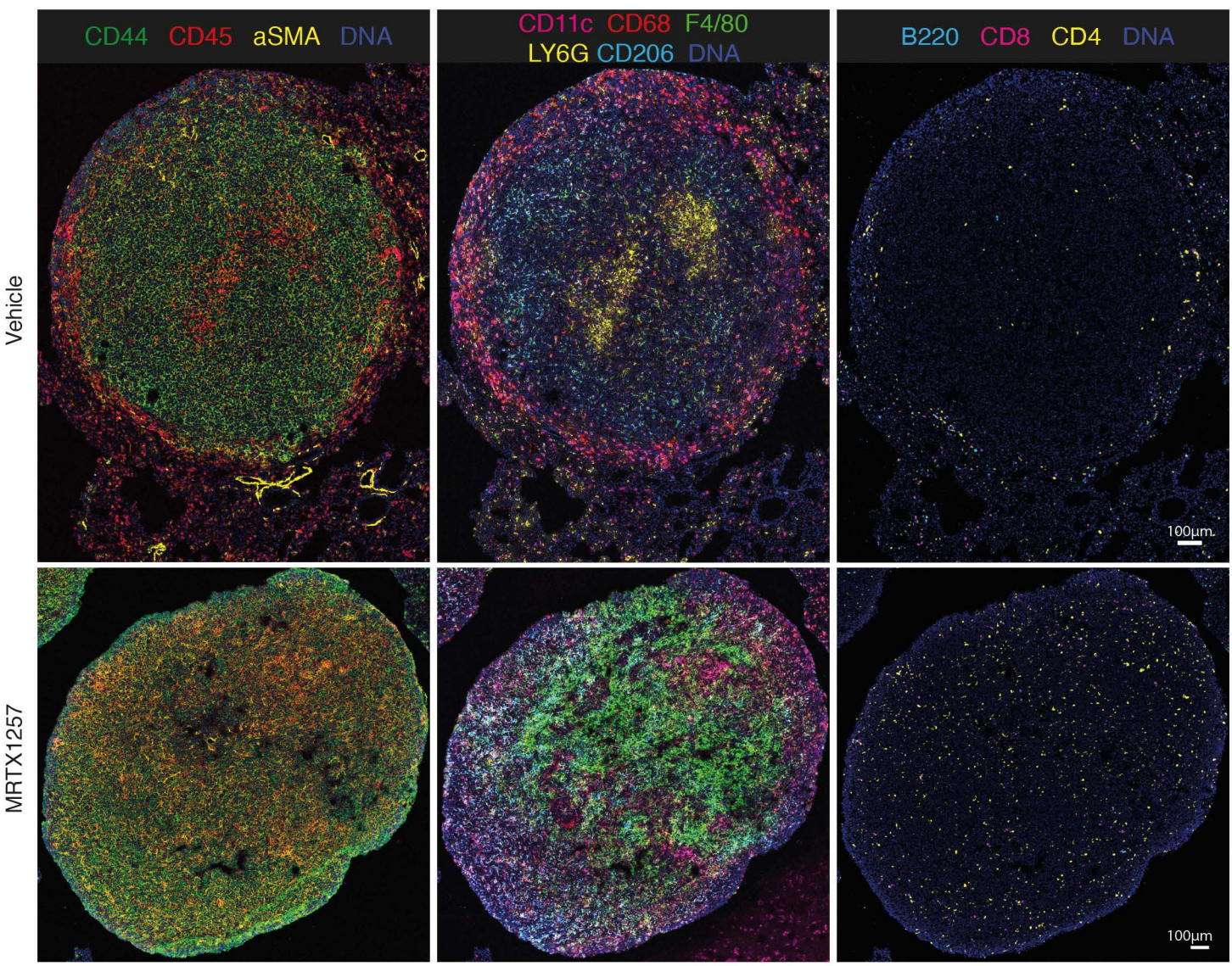

Figure 1

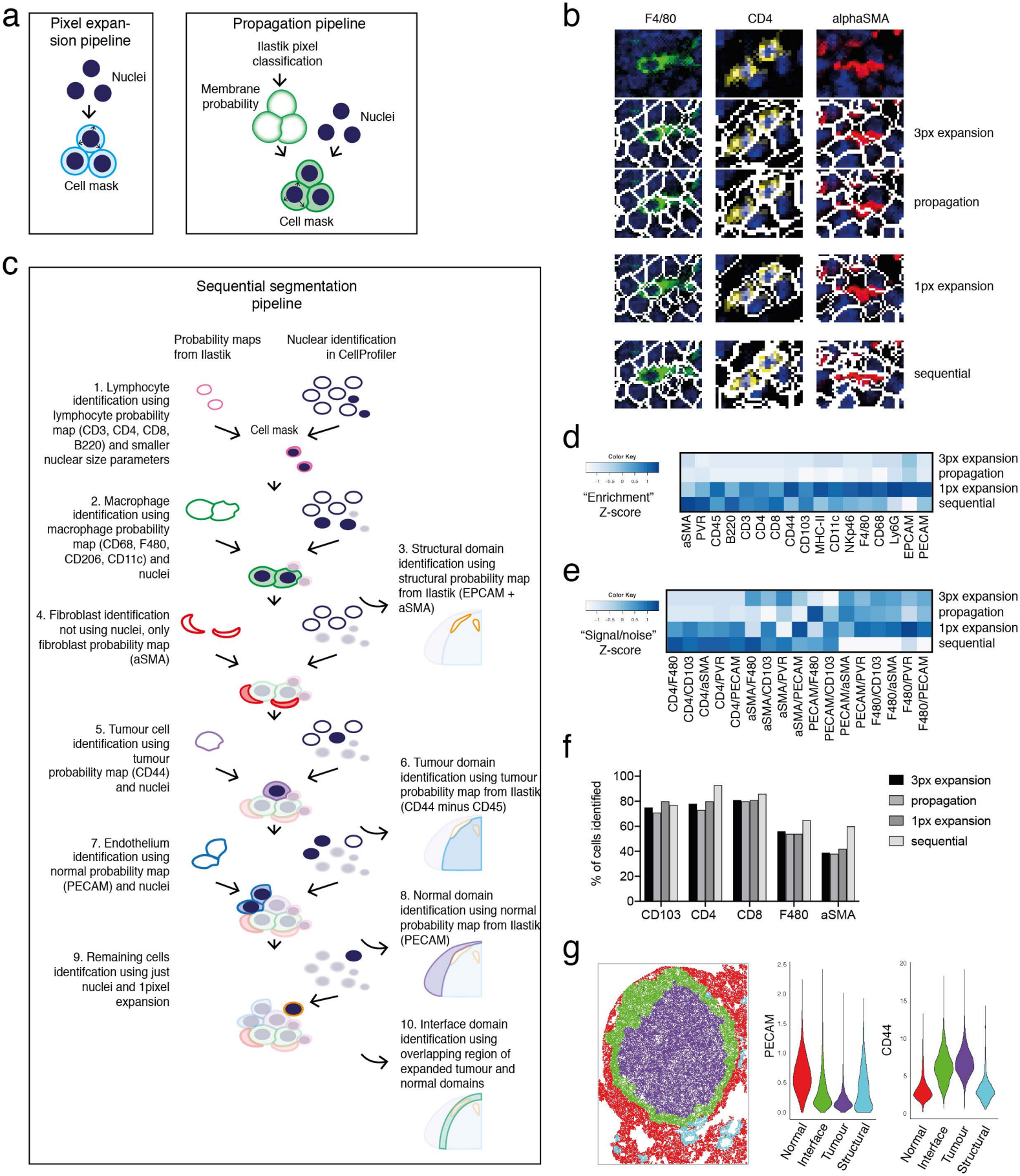
a
Pixel expan-
sion pipeline
Nuclei
Cell mask
Propagation pipeline
Ilastik pixel
classification
Membrane
probability
Nuclei
Cell mask
b
F4/80
CD4
alphaSMA
3px expansion
propagation
1px expansion
sequential
c
Sequential segmentation
pipeline
Probability maps
from Ilastik
Nuclear identification
in CellProfiler
1. Lymphocyte identification using lymphocyte probability map (CD3, CD4, CD8, B220) and smaller nuclear size parameters
Cell mask
2. Macrophage identification using macrophage probability map (CD68, F480, CD206, CD11c) and nuclei
3. Structural domain identification using structural probability map from Ilastik (EPCAM + aSMA)
4. Fibroblast identification not using nuclei, only fibroblast probability map (aSMA)
5. Tumour cell identification using tumour probability map (CD44) and nuclei
6. Tumour domain identification using tumour probability map from Ilastik (CD44 minus CD45)
7. Endothelium identification using normal probability map (PECAM) and nuclei
8. Normal domain identification using normal probability map from Ilastik (PECAM)
9. Remaining cells identifcation using just nuclei and 1pixel expansion
10. Interface domain identification using overlapping region of expanded tumour and normal domains
d
Color Key
"Enrichment"
Z-score
3px expansion
propagation
1px expansion
sequential
aSMA
PVR
CD45
B220
CD3
CD4
CD8
CD44
CD103
MHC-II
CD11c
NKp46
F4/80
CD68
Ly6G
EPCAM
PECAM
e
Color Key
"Signal/noise"
Z-score
3px expansion
propagation
1px expansion
sequential
CD4/F480
CD4/CD103
CD4/aSMA
CD4/PVR
CD4/PECAM
aSMA/F480
aSMA/CD103
aSMA/PVR
aSMA/PECAM
PECAM/F480
PECAM/CD103
PECAM/aSMA
PECAM/PVR
F480/CD103
F480/aSMA
F480/PVR
F480/PECAM
f
% of cells identified
100
80
60
40
20
0
CD103
CD4
CD8
F480
aSMA
3px expansion
propagation
1px expansion
sequential
g
PECAM
CD44
Normal
Interface
Tumour
Structural

Figure 2

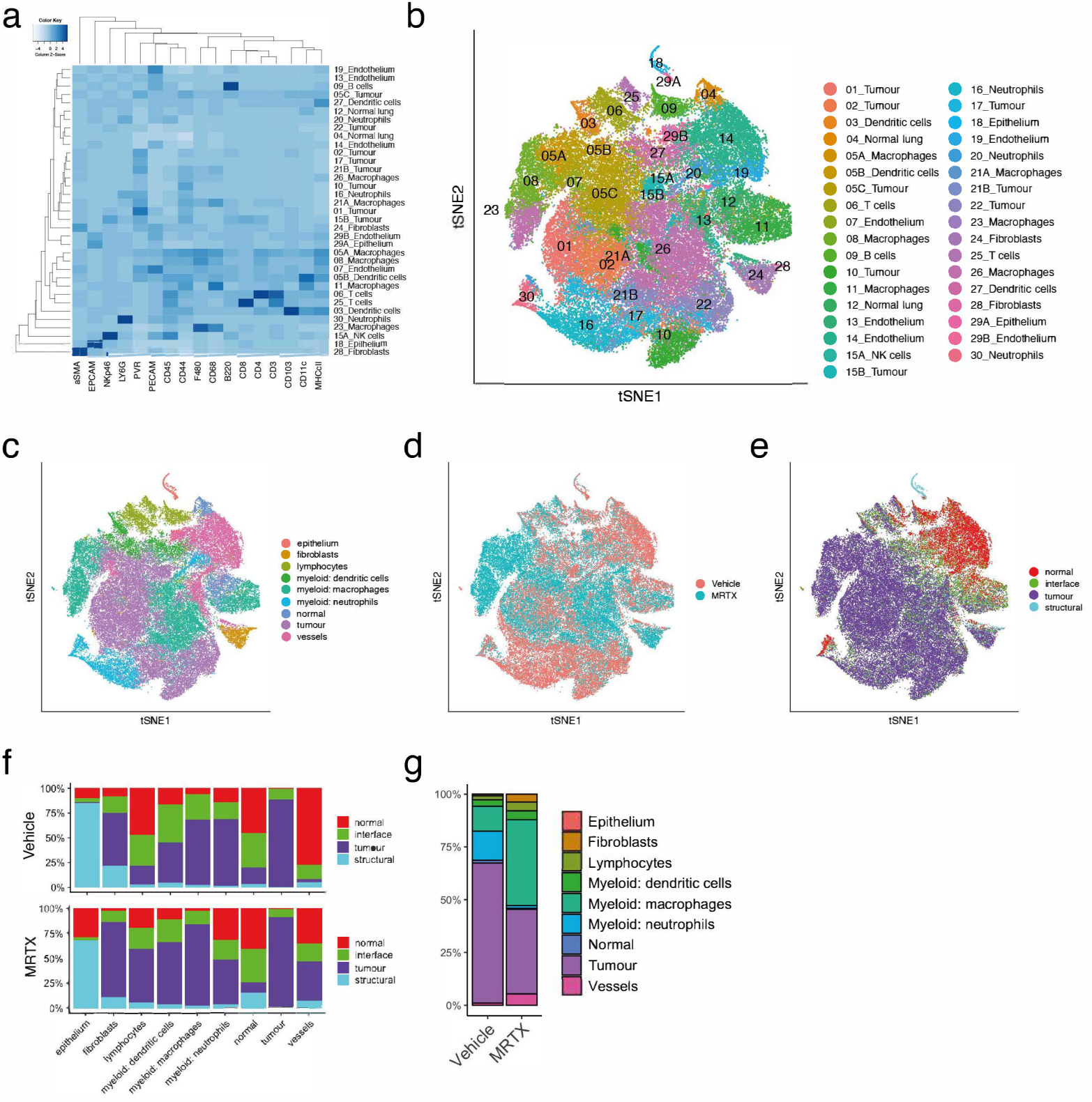
a
Color Key
Column Z-Score
19_Endothelium
13_Endothelium
09_B cells
05C_Tumour
27_Dendritic cells
12_Normal lung
20_Neutrophils
22_Tumour
04_Normal lung
14_Endothelium
02_Tumour
17_Tumour
21B_Tumour
26_Macrophages
10_Tumour
16_Neutrophils
21A_Macrophages
01_Tumour
15B_Tumour
24_Fibroblasts
29B_Endothelium
29A_Epithelium
05A_Macrophages
08_Macrophages
07_Endothelium
05B_Dendritic cells
11_Macrophages
06_T cells
25_T cells
03_Dendritic cells
30_Neutrophils
23_Macrophages
15A_NK cells
18_Epithelium
28_Fibroblasts
aSMA
EPCAM
NKp46
LY6G
PVR
PECAM
CD45
CD44
F480
CD68
B220
CD8
CD4
CD3
CD103
CD11c
MHCcII
b
tSNE2
tSNE1
01_Tumour
02_Tumour
03_Dendritic cells
04_Normal lung
05A_Macrophages
05B_Dendritic cells
05C_Tumour
06_T cells
07_Endothelium
08_Macrophages
09_B cells
10_Tumour
11_Macrophages
12_Normal lung
13_Endothelium
14_Endothelium
15A_NK cells
15B_Tumour
16_Neutrophils
17_Tumour
18_Epithelium
19_Endothelium
20_Neutrophils
21A_Macrophages
21B_Tumour
22_Tumour
23_Macrophages
24_Fibroblasts
25_T cells
26_Macrophages
27_Dendritic cells
28_Fibroblasts
29A_Epithelium
29B_Endothelium
30_Neutrophils
c
tSNE2
tSNE1
epithelium
fibroblasts
lymphocytes
myeloid: dendritic cells
myeloid: macrophages
myeloid: neutrophils
normal
tumour
vessels
d
tSNE2
tSNE1
Vehicle
MRTX
e
tSNE2
tSNE1
normal
interface
tumour
structural
f
Vehicle
MRTX
100%
75%
50%
25%
0%
normal
interface
tumour
structural
epithelium
fibroblasts
lymphocytes
myeloid: dendritic cells
myeloid: macrophages
myeloid: neutrophils
normal
tumour
vessels
g
100%
75%
50%
25%
0%
Vehicle
MRTX
Epithelium
Fibroblasts
Lymphocytes
Myeloid: dendritic cells
Myeloid: macrophages
Myeloid: neutrophils
Normal
Tumour
Vessels

Figure 3

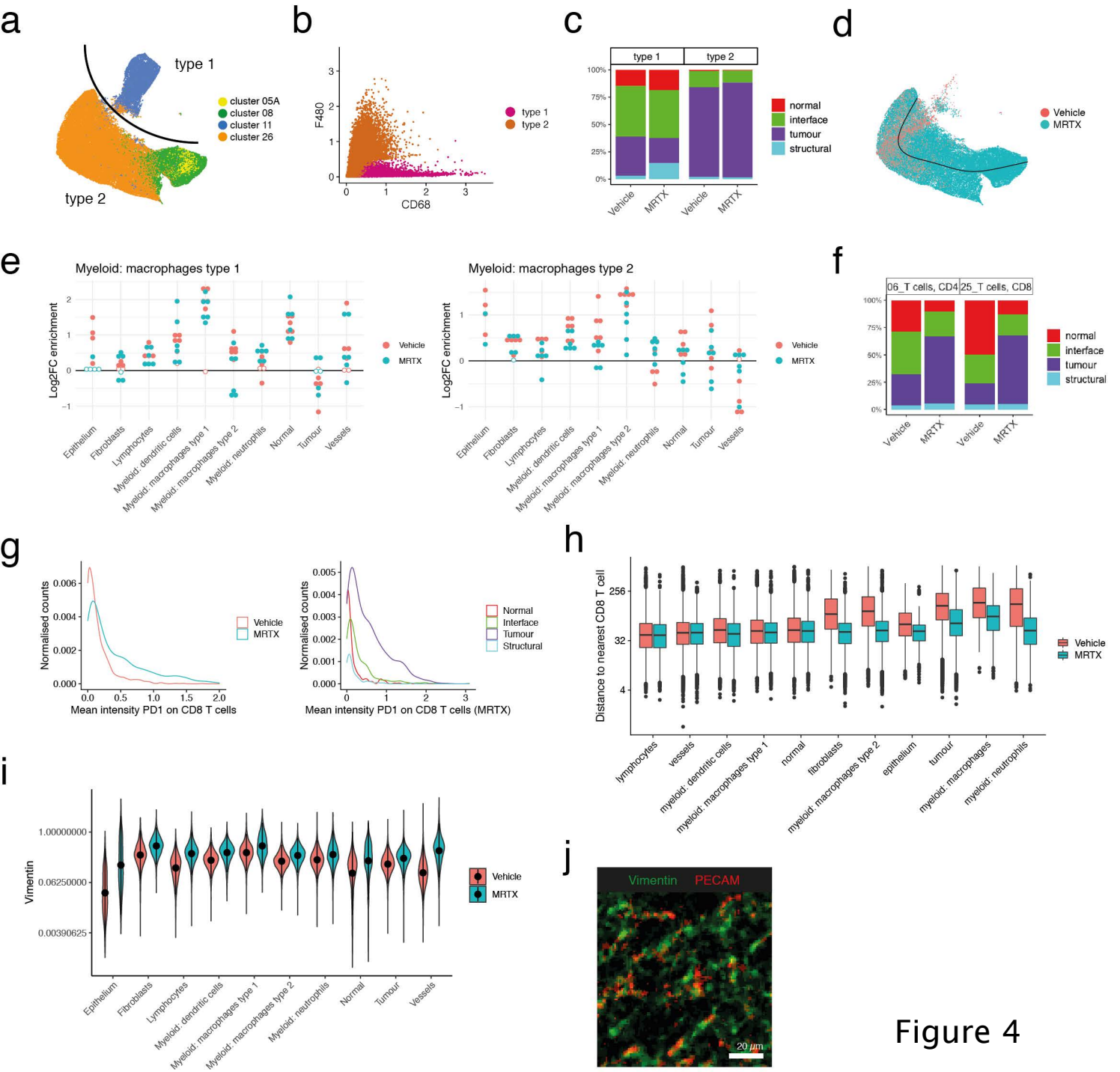
a
type 1
type 2
cluster 05A
cluster 08
cluster 11
cluster 26
b
F480
CD68
type 1
type 2
c
type 1
type 2
normal
interface
tumour
structural
Vehicle
MRTX
d
Vehicle
MRTX
e
Myeloid: macrophages type 1
Myeloid: macrophages type 2
Log2FC enrichment
Epithelium
Fibroblasts
Lymphocytes
Myeloid: dendritic cells
Myeloid: macrophages type 1
Myeloid: macrophages type 2
Myeloid: neutrophils
Normal
Tumour
Vessels
f
06_T cells, CD4
25_T cells, CD8
g
Normalised counts
Mean intensity PD1 on CD8 T cells
Mean intensity PD1 on CD8 T cells (MRTX)
Normal
Interface
Tumour
Structural
h
Distance to nearest CD8 T cell
i
Vimentin
j
Vimentin
PECAM
20 μm

Figure 4